Geophysical Research Letters

RESEARCH LETTER
10.1029/2023GL105652

Key Points:

- Wind spectrum density from wind profiler radars over China shows a less negative slope over inland sites than the −5/3 power law over ocean
- Temporal and spatial variation of maximum wind speed in the lower troposphere and low level jets are characterized
- Wind spectrum from ERA5 reanalysis is realistic (deficient) for time scales >1 day (<1 day) compared with profiler data

Supporting Information:

Supporting Information may be found in the online version of this article.

Correspondence to:

Y. Wang and X. Xu,
wyj@cma.gov.cn;
xuxd@cma.gov.cn

Citation:

Wang, Y., Zeng, X., Xu, X., Galarneau, T. J., Jr., Li, F., & Zhao, Y. (2024). Power spectra and diurnal variation of low-level horizontal winds observed by a wind profiler radar network over China. *Geophysical Research Letters*, *51*, e2023GL105652. https://doi.org/10.1029/2023GL105652

Received 27 JUL 2023
Accepted 7 JAN 2024

Author Contributions:

Conceptualization: Yinjun Wang, Xubin Zeng
Data curation: Yinjun Wang, Feng Li
Funding acquisition: Xiangde Xu
Software: Yinjun Wang, Feng Li, Yang Zhao
Supervision: Xiangde Xu
Writing – original draft: Yinjun Wang, Xubin Zeng
Writing – review & editing: Yinjun Wang, Xubin Zeng, Xiangde Xu, Thomas J. Galarneau Jr.

Power Spectra and Diurnal Variation of Low-Level Horizontal Winds Observed by a Wind Profiler Radar Network Over China

Yinjun Wang[1,2], Xubin Zeng[2], Xiangde Xu[1], Thomas J. Galarneau Jr.[3], Feng Li[1], and Yang Zhao[4,5]

[1]State Key Laboratory of Severe Weather, Chinese Academy of Meteorological Sciences, Beijing, China, [2]Department of Hydrology and Atmospheric Sciences, University of Arizona, Tucson, AZ, USA, [3]NOAA/OAR National Severe Storms Laboratory, Norman, OK, USA, [4]Frontier Science Centre for Deep Ocean Multispheres and Earth System and Physical Oceanography Laboratory, Ocean University of China, Qingdao, China, [5]College of Oceanic and Atmospheric Sciences, Ocean University of China, Qingdao, China

Abstract Understanding the diurnal variation of horizontal wind in the atmospheric boundary layer is important for weather and climate research and wind energy applications. Here we analyze the hourly data from 91 wind profiler radar sites in China and observe that the power spectral density of horizontal wind in lower troposphere approximately follows the −5/3 power law in the mesoscale range over the ocean and coastal areas. However, in inland areas, the slopes of the power spectra are significantly greater than −5/3. We characterize the temporal and spatial variations of maximum wind speed and low level jets and find that the thermal wind effect may partially contribute to the high percentage of low-level jets observed in the southeastern coast of China and Hainan Island. While the ERA5 reanalysis reproduces wind spectrum well for time scales >1 day, its spectrum diverges significantly from that of profiler data at shorter time scales.

Plain Language Summary Understanding how the horizontal wind changes throughout the day in the lower part of the atmosphere is important for studying weather and climate and using wind energy. In this study, we looked at data from 91 radar sites in China that measure wind every hour. We found that the pattern of how the wind changes follows a specific mathematical relationship, called a power law, where the wind decreases in a particular way with decreasing spatial and temporal scales. This pattern holds true mostly over the ocean and coastal areas, but in areas further inland, the wind behaves a bit differently. We also studied how the low-level jet (LLJ), which are fast winds at low altitudes, change over time and space. We discovered that the difference in temperature across the region contributes to the occurrence of these LLJs in coastal areas in southeast China and Hainan Island. Finally, we compare our findings with the ERA5 reanalysis, which demonstrates excellent agreement in reproducing the wind spectrum for time scales greater than 1 day. However, the spectrum derived from the ERA5 reanalysis diverges significantly from the profiler data at shorter time scales.

1. Introduction

Analysis of wind variability in the frequency or wavenumber domain provides important information for various applications, such as dynamic wind loading and turbulent diffusion of atmospheric constituents (Larsén et al., 2016). The wind velocity spectrum can be affected by many factors (e.g., sea breeze, boundary-layer rolls and swell waves; Heggem et al., 1998; Högström et al., 2015; Smedman, 1991). While previous studies have examined the velocity spectrum in different frequency bands from 10^{-8}–1 Hz for application demands for wind engineering and numerical forecasting (Sim et al., 2023), the characteristics and cause of the wind velocity spectrum, particularly in the mesoscale range, continue to be controversial (Y. Wang et al., 2018). For instance, using the aircraft data near the tropopause, Lindborg (1999) pointed out that the slope of wind velocity spectrum (of −3) appears for smaller wavenumbers (and frequency) than that of −5/3 in the double logarithm coordinate, which are contrary to the theoretical prediction for isotropic 2D turbulence. Previous studies show the characteristics of wind velocity spectrum in mesoscale range may be explained by stratified turbulence or cascades of inertia gravity waves (Callies et al., 2014), but it is not clear if differences exist between the wind velocity spectrum in the lower troposphere above different underlying surfaces. Nastrom et al. (1987) demonstrated that the spectra in the mesoscale range are up to six times larger in mountainous regions compared to flat terrain, likely due to the

presence of more inertia-gravity waves over rolling topography. The scarcity of quality mesoscale observations in complex terrain contributes to the uncertainty in the characteristics and causes of the wind velocity spectrum (e.g., Koch et al., 2018; Yepes et al., 2019).

While the temporal variability of wind can be characterized by the spectrum, the vertical variability of mesoscale wind in the lower troposphere includes the low-level jet (LLJ), or low-level wind maximum (e.g., Gutierrez et al., 2016; Smedman et al., 1995). The LLJ can have an important impacts on, for example, aviation safety (Kaplan et al., 2000), atmospheric environment (Miao et al., 2018), severe thunderstorm occurrence (e.g., Bonner et al., 1968), and wind energy applications (Storm et al., 2009). Blackadar (1957) proposed that the LLJ is often associated with supergeostrophic wind at night, and its formation is attributed to the inertial oscillation that occurs in response to an imbalance of the pressure gradient, friction, and Coriolis forces. The force imbalance is triggered by the decoupling of the boundary layer from the surface layer due to longwave radiative cooling after sunset that reduces the effect of friction (Markowski & Richardson, 2010). Subsequent studies found the other mechanisms that give rise to the LLJ, such as differential cooling over sloping terrain (Parish & Oolman, 2010), sea-land thermal contrast (Ranjha et al., 2013), local thermally induced forcing (Walters et al., 2008), and coupling to upper-level jets (Burrows et al., 2020). The physical mechanisms and characteristics for LLJs varies geographically across the globe (Rife et al., 2010).

The wind spectrum and LLJs over China have also been studied in the past. For instance, through numerical simulations, Du et al. (2014) found that the northeast cold vortex, characterized by a closed cyclonic circulation and a cold core at mid-levels, plays a key role in the higher occurrence frequency of LLJs over northeastern China and the north plain region. Li et al. (2021) investigated the full-scale wind speed spectra of 5 year time series in Beijing from meteorological tower, and Miao et al. (2018) analyzed the climatology of LLJ by combining WPR and numerical simulation in Beijing and Guangzhou.

Here we use the unique observational data from a WPR network and the fifth generation ECMWF atmospheric reanalysis of the global climate (ERA5 reanalysis; Hersbach et al., 2020) to examine the characteristics of the lower tropospheric wind power spectra and LLJ in China. The purpose of this study is to reveal the horizontal and vertical variation of wind velocity spectrum at different underlying surfaces (e.g., land, ocean, and coast) in the lower troposphere and analyze the characteristics of temporal and spatial variation and formation mechanisms of the LLJ in China. The observational data and analysis methods are described in Section 2. The wind velocity spectrum in the synoptic and mesoscale range is analyzed in Section 3.1, and the formation mechanism and spatial-temporal characteristics of the LLJ are presented in Section 3.2. Further discussions are given in Section 3.3, and conclusions are provided in Section 4.

2. Data and Method

In this study, we use hourly average WPR data with high vertical resolution (~100 m) from 91 China Meteorological Administration (CMA) operational stations in 2019 (Liu et al., 2020). The WPR uses five beams, including one vertical and four off-vertical beams, and the angle between vertical and off-vertical beams is about 15°. According to the design criterion for WPR in China, the wind speed and wind direction errors are less than 1.5 m s^{-1} and 10° from 0.1 to 2.5 km above ground level (AGL). The original temporal resolution of the WPR raw data is about 5–6 min, and the quality controlled raw data is used to obtain hourly average winds. The WPR data is compared to radiosonde data from three CMA operational stations (Guo et al., 2016; Zhang et al., 2018) and the hourly ERA5 pressure-level data available every 25 hPa below 750 hPa and at 0.25° latitude-longitude grid spacing. The ERA5 does not assimilate information from the WPR network. The pressure-level winds are linearly interpolated (using geopotential heights at pressure levels) to heights consistent with the WPR data.

The power spectra of horizontal wind in the lower troposphere are calculated for the WPR and ERA5 from January to August in 2019. We did not calculate the power spectra for the full year because the WPR data was frequently missing at some sites in September through November in 2019. The horizontal wind speed from WPR data was calculated at 0.1, 0.2, 0.4, 0.7, 1.0, and 2.0 km AGL for the power spectral analysis. Here we use linear temporal interpolation to fill in missing data before the linear detrending is applied. In order to reduce the variance of power spectral density, Welch's overlapped segment averaging estimator is used to obtain the power spectral density estimate (Welch, 1967). This technique involves dividing the time series into overlapping segments and a Hamming window is applied to each segment. A segment length of 100 samples is used with 50 overlapped

samples and a discrete Fourier transform length of 1,024 points. A modified periodogram is computed for each segment and these estimates are averaged to produce the estimate of the power spectral density.

To examine the impact of elevation, topographic relief, and variations in underlying surface between land and water on power spectra, we selected five representative WPR sites (see Table S1 and Figure S1 in Supporting Information S1). These sites include three locations in the mid-latitudes: a high-elevation site (Gangcha), a North China Plain site (Beijing), and a site with high topographic relief (Zigui). Additionally, we chose two locations in the lower latitudes: a coastal site (Shenzhen) and a small island site (Xisha). At each site, we analyzed the hourly WPR data from January to August 2019 to determine the maximum wind speed within a 24-hr period at five different heights (0.1, 0.3, 0.7, 1.0, and 2.0 km). Additionally, following Whiteman et al. (1997) and Wei et al. (2014), LLJs were identified using the wind speed profile below 3 km AGL. The nose of the LLJ was defined where the maximum wind speed $\geq$10 m s^{-1} and the difference in wind speed between the maximum wind speed and the minimum speed above the LLJ nose must $\geq$5 m s^{-1}.

3. Results

3.1. Power Spectra of Horizontal Wind

The power spectra of horizontal wind are computed using the hourly WPR data with a focus on the frequency (f) range from 3×10^{-7}–1.3×10^{-5} Hz which corresponds to a period ranging from about 1 month to 2 hr. This frequency range is further divided into three subranges. The extended to subseasonal range (Range-1) is defined as 3×10^{-7} Hz $< f < 1 \times 10^{-6}$ Hz (or for periods of 12 days to 1 month). The upper mesoscale and synoptic-scale range (Range-2) is defined as 3×10^{-6} Hz $< f < 2 \times 10^{-5}$ Hz (or from about 14 hr to 4 days). Finally, the mesoscale range (Range-3) is defined here as 2×10^{-5} Hz $< f < 1.3 \times 10^{-5}$ Hz (or for about 2–14 hr). For each frequency range, the spectrum density $S(f)$ is computed to represent the power spectra of horizontal wind and the integration of $S(f)$ with respect to frequency f equals the variance of horizontal wind. If $S(f)$ is proportional to f^{α}, then α represents the slope in the relation between the logarithms of $S(f)$ and f.

Figure 1a displays the slopes derived from the spectrum density obtained from the WPR, $S_{\mathrm{WPR}}(f)$, at a height of 1.0 km AGL for nearly all 91 sites. These slopes fall within −0.15 to 0 in Range-1, indicating a slight decrease of $S(f)$ as f increases. Figure 2 shows that the above result remains largely consistent from 0.1 to 2.0 km AGL. The slopes of all five sites fall within −0.15 to 0 in Range-1. These findings align with the near zero slope from cup and sonic anemometer measurements within the surface layer (Larsén et al., 2018) and in the lower boundary layer (∼280 m; based on a meteorological tower in Beijing) (Li et al., 2021).

Due to a strong diurnal peak at a frequency of 1 day^{-1} in $S(f)$, we adopt the approach introduced by Larsén et al. (2018) and exclude samples near 1 day^{-1} (0.9–1.1 day^{-1}) before calculating the slopes of $S(f)$ in Range-2. Generally, at the height of 1 km AGL, the slopes of $S_{\mathrm{WPR}}(f)$ in Range-2 are mostly greater than −5/3 (Figure 1b). For the northern region of China (110°E–125°E, 33°N–44°N), the mean slope of $S_{\mathrm{WPR}}(f)$ in Range-2 is −1.13, while for the southern region (110°E–125°E, 22°N–33°N) it is −1.3, which is closer to −5/3. The slopes of $S_{\mathrm{WPR}}(f)$ in Range-2 approximately adhere to the $f^{-5/3}$ power law at the Shenzhen coastal site and Xisha small island site (Figure 2). However, at the other three inland sites, the slopes (ranging from −1.3 to −0.8) are significantly greater than −5/3. At the Xisha site, the slopes of $S_{\mathrm{WPR}}(f)$ in Range-2 remain relatively consistent with height, while at the other four sites they decrease with increasing height (Figure S2a in Supporting Information S1). According to theoretical predictions for quasi-2D geostrophic turbulence, the slope of $S(f)$ in Range-2 should be close to −3. Figure 2 demonstrates that the f^{-3} scaling is evident for f from approximately 3×10^{-6} Hz to 8×10^{-6} Hz at Shenzhen and Xisha sites. However, this scaling is not apparent at the other three inland sites, where the assumption of quasi-2D geostrophic turbulence may not be valid for the lowest 2 km of the atmosphere.

Figure 1c shows that the slopes of $S_{\mathrm{WPR}}(f)$ at 1.0 km AGL in Range-3 are predominantly greater than −5/3 across most sites. Specifically, at the Shenzhen site, the slopes of $S_{\mathrm{WPR}}(f)$ in Range-3 are approximately −5/3, whereas at the other four sites the slopes are significantly greater than −5/3 (Figure S2b). While the slopes are relatively consistent with height in Range-3 (Figure 2 and Figure S2b in Supporting Information S1), $S_{\mathrm{WPR}}(f)$ at most sites, except the Zigui site, increase with height in Range-1 and Range-2 (Figure 2). Based on the power spectra of horizontal wind from the Nysted and Horns Rev sites in Denmark, Larsén et al. (2013) proposed a fitting function called $S_L(f)$ over water for periods from several days to about 10 min Figure 2 shows that $S_L(f)$ provides a good fit for the Xisha site at all five heights from approximately 3×10^{-6} Hz to 6×10^{-5} Hz. However, at the other four

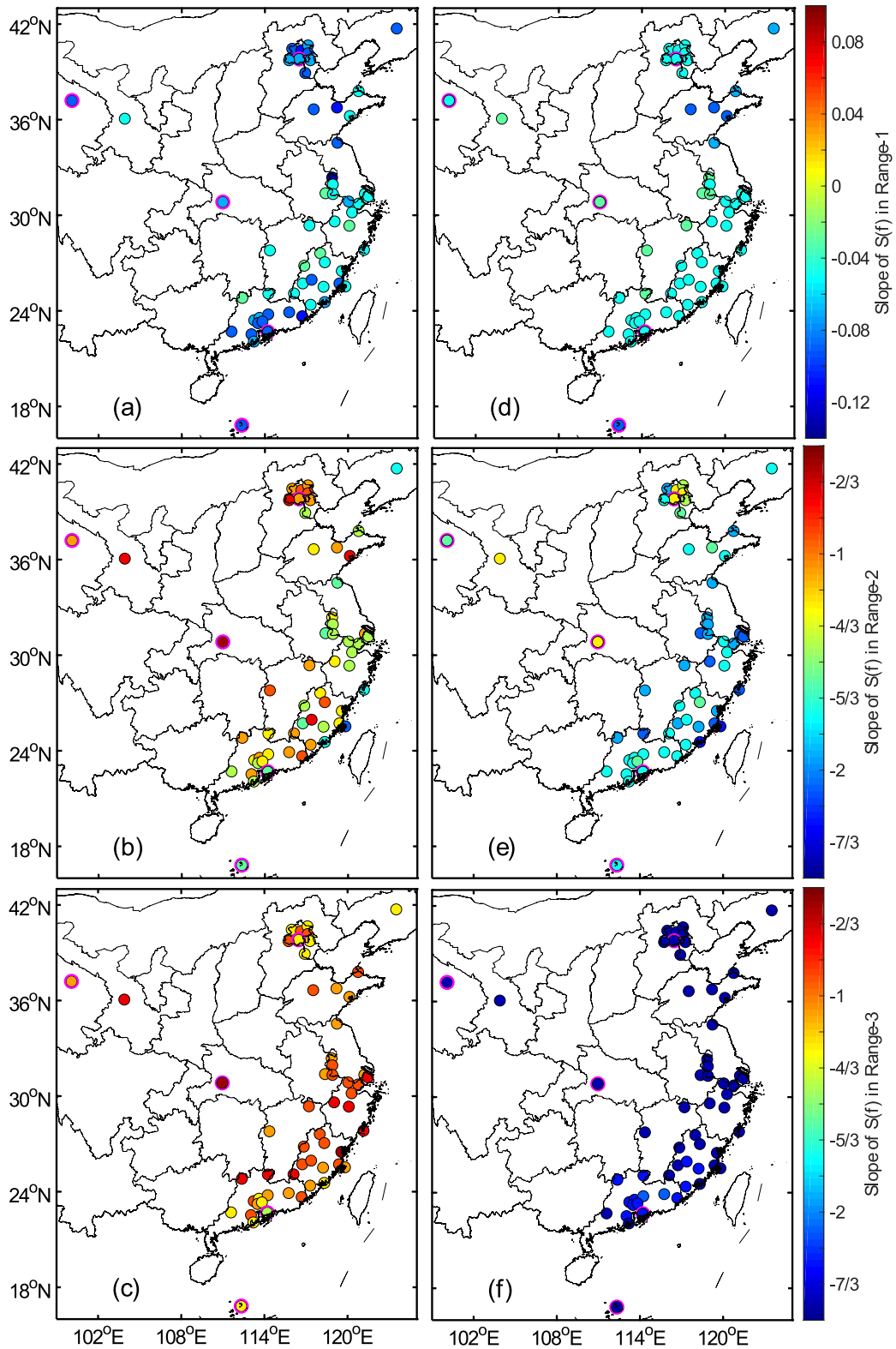

Figure 1. Slope (shaded according to the colorbar) of $S_{WPR}(f)$ at 1 km above ground level for each wind profiler radar (WPR) site at (a) Range-1, (b) Range-2, and (c) Range-3 frequencies from January to August in 2019. Panels (d)–(f) as in panels (a)–(c), except for $S_{EC}(f)$. The five representative WPR sites are marked by magenta circles.

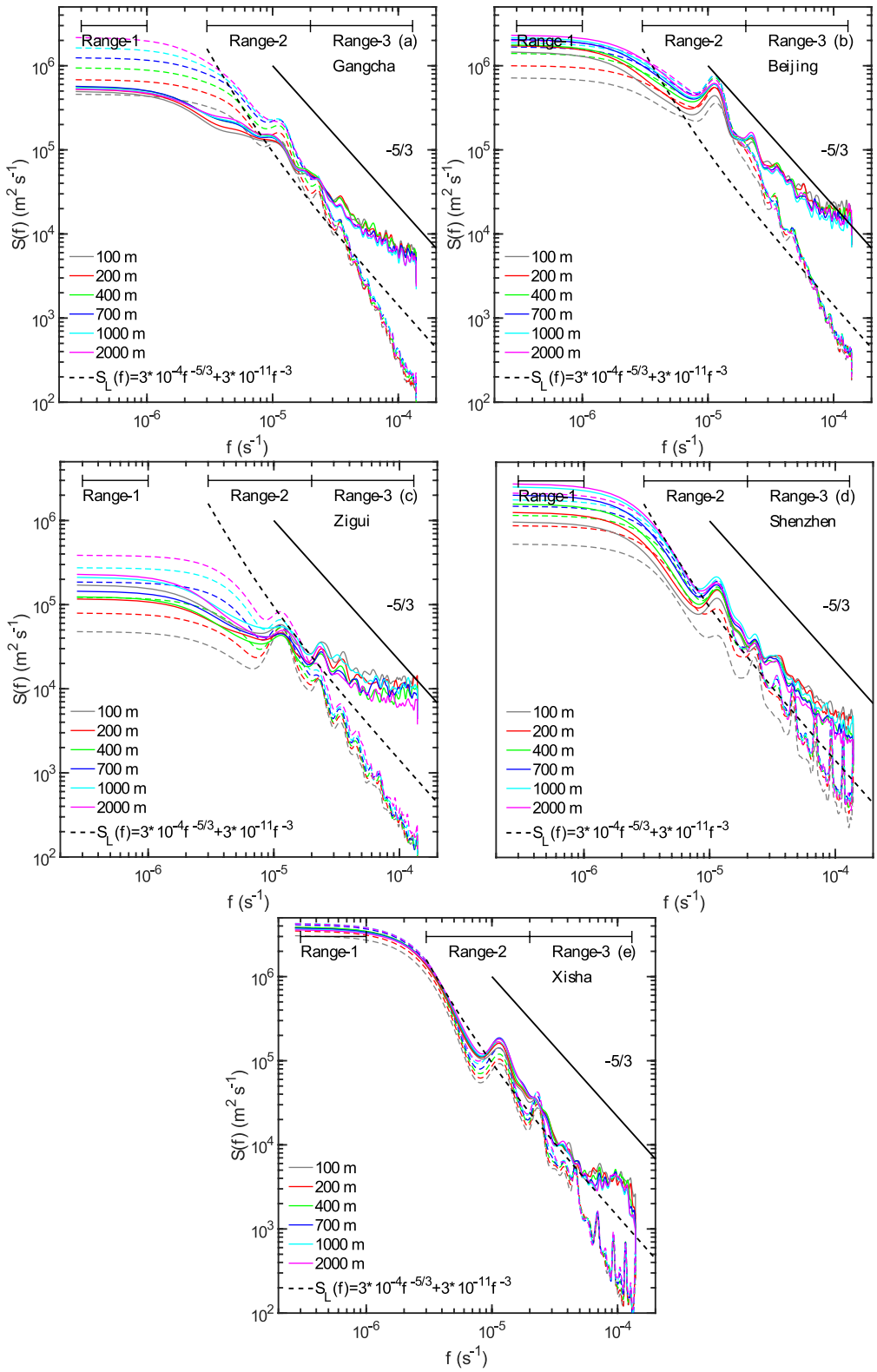

Figure 2. The power spectra, $S(f)$, of horizontal wind at 0.1 (gray), 0.2 (red), 0.4 (green), 0.7 (blue), 1 (cyan), and 2 (magenta) km above ground level for (a) Gangcha, (b) Beijing, (c) Zigui, (d) Shenzhen, and (e) Xisha from January to August 2019. $S_{WPR}(f)$ is shown in solid colored lines, $S_{EC}(f)$ in dashed colored lines, and $S_L(f)$ in a dashed black line. The slope of −5/3 is represented by the solid black line. The Range-1, -2, and -3 are located across the x axis at the top of each panel.

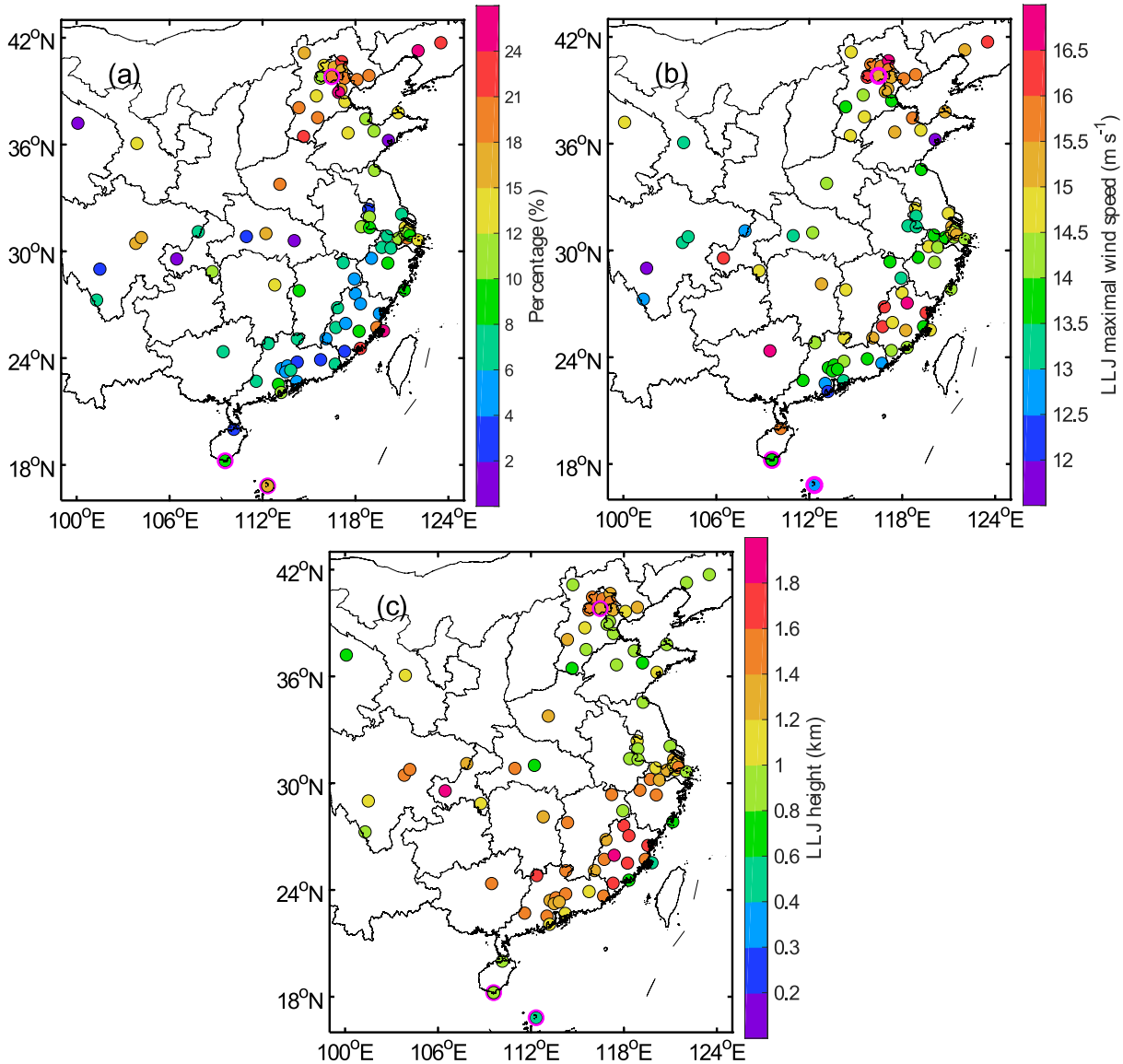

Figure 3. The (a) frequency of occurrence of low level jets (LLJs) (shaded in %), (b) mean maximum wind speed at the LLJ nose (shaded in m s^{-1}), and (c) mean height of LLJ noses (shaded in km) for all LLJs identified throughout the day for each wind profiler radar site from January to August in 2019 in China. The three sites in Figure S7 in Supporting Information S1 are marked by magenta circles.

inland or coastal sites, $S_{WPR}(f)$ significantly deviates from the $S_L(f)$ in this range, with $S_{WPR}(f)$ in Range-3 being two to five times greater than $S_L(f)$.

3.2. Low Level Jet

Due to the sparse distribution of WPR sites in western China, our analysis primarily focuses on the spatial distribution of the mean percentage of LLJ occurrences, maximum wind speed, and height of LLJ noses in eastern China. Figure 3a shows that the percentages of LLJ occurrences generally range from 10% to 24% north of 35°N, with higher occurrences observed in this region compared to south of 35°N. The higher occurrence frequency of LLJs over northeastern China and the north plain region (35°N–60°N, 115°E−145°E) is closely associated with the northeast cold vortex, as demonstrated in the numerical simulations of Du et al. (2014). The spatial distribution of LLJ occurrences shown in Figure 3a corresponds well with previous findings based on radiosonde data (Yan et al., 2021) and it also corresponds to that of the mean surface wind speed patterns

(Climatological Atlas, 2002). However, the percentages shown in Figure 3a are generally lower by approximately 20% compared to the radiosonde data. This discrepancy can be attributed to various factors such as the difference in data sampling frequency (hourly WPR data vs. twice-daily radiosonde data), distinct locations, seasonal variation, varying time durations of the two data sets, and measurement differences. In southern China, higher percentages are observed along the southeast coast and nearby islands (e.g., Fujian coastal area and Xisha island). These coastal and island sites exhibit percentages >15%, while inland sites typically range from 4% to 12%. We will further analyze these results for the two island sites later.

At most sites in the north plain and northeast regions, the maximum wind speeds of LLJ noses are approximately 15–16.5 m s^{-1}, whereas other regions generally do not exceed 15 m s^{-1} (Figure 3b). The spatial distribution of maximum wind speeds is consistent with findings based on radiosondes (Yan et al., 2021). The inland areas of southern China have many sites with the altitude of LLJ noses exceeding 1.2 km AGL (Figure 3c), and our WPR results generally indicate a 20% higher elevation compared to radiosonde data (Yan et al., 2021).

To examine diurnal aspects of the maximum wind speed, we utilize the hourly WPR data from January to August in 2019. We determine the local time (defined here as UTC + 8) maximum wind speed for each day and then calculate the most frequent local time and average maximum wind speed at 1 and 2 km AGL for each site (Figure 4a and Figure S3a in Supporting Information S1). The frequency distributions of most frequent local time at these two heights, as well as 0.1 km, 0.3 and 0.7 km AGL, are presented in Figure 4b. The most frequent local time at 0.3, 0.7, and 1.0 km AGL is around 9 a.m. (Figure 4b). This is primarily influenced by sites located in southeastern coastal areas (Figure 4a). However, at 0.1 and 2 km AGL, the most frequent local time exhibits a bimodal distribution with peaks around 9 a.m. and 9 p.m. (Figure 4b), and there is no obvious coherent pattern in the spatial distribution of the average local time (Figure 4a). These results align with previous findings using WPR data from November 2018 to March 2019 (Liu et al., 2020).

Alternatively, we can compute statistics by first calculating the average diurnal cycle of hourly wind speed for each site and then determining the local time and magnitude of the maximum hourly mean wind speed at 1 and 2 km AGL (Figure 4c and Figure S3b in Supporting Information S1). The corresponding frequency distributions of the local time for these two heights, as well as 0.1 km, 0.3 and 0.7 km AGL, are shown in Figure 4d. The results computed using this method differ from those presented in Figures 4a and 4b. For instance, the maximum hourly mean wind speeds in Figure 4c are approximately two-thirds of those in Figure 4a for most sites. At 0.7, 1, and 2 km AGL, the most frequent local time spans from 10:30 p.m. to 4:30 a.m. (Figure 4d). From northern to southern China, the local time associated with the maximum wind speed generally shifts from around midnight to 9 a.m. (Figure 4c). This gradual shift may be linked to the LLJ induced by the inertial oscillation (Blackadar, 1957; Shapiro & Fedorovich, 2010; Shapiro et al., 2016). The inertial period is inversely proportional to the Coriolis parameter, hence increasing with decreasing latitude. Consequently, the maximum wind speed occurrence in southern China is delayed compared to the timing observed in northern China.

To better understand the formation mechanism of LLJs, we examine the evolution of the winds the Sanya and Haikou coastal sites on 18–19 October 2019. Northeasterly flow persisted below 2 km AGL at both Haikou and Sanya (Figure S4 in Supporting Information S1). However, a mesoscale LLJ was occurred at Sanya in the evening from about 7 to 11 p.m. local time on both days. Why was a LLJ present at Sanya, but not at Haikou? One possibility is related to enhanced northeasterly flow associated with differential heating over elevated terrain. Differential heating over elevated terrain in southwestern Hainan Island resulted in a mesoscale high temperature center evident at the 925 and 975 hPa pressure level at 4 p.m. on 18 October (Figure S5 in Supporting Information S1). The northwestward-directed temperature gradient resulted in a northeasterly thermal wind of about 5 m s^{-1} by 8 p.m. (Figure S6 in Supporting Information S1). The northeasterly thermal wind added on to the background synoptic-scale northeasterly flow and resulted in the LLJ observed at Sanya. At Haikou, however, the relatively weak thermal wind has a much smaller impact on the synoptic-scale northeasterly flow. Later on in the overnight hours after midnight, however, the boundary layer height decreases due to nocturnal cooling leading to the disappearance of turbulent friction force above the stable boundary layer. Characteristic of the inertial oscillation, a LLJ develops as the winds become supergeostrophic in the absence of friction (Figure S4 in Supporting Information S1). A similar evolution occurs the following day on 19 October.

As mentioned in Section 3.1, some of our findings derived from WPR data differ from previous studies based on radiosonde data. To better understand these differences, we compare the WPR wind speeds (WS_{wpr}) at three sites (inland—Beijing, coastal—Sanya, and small island—Xisha) with the radiosonde data (WS_{rad}) at nearby

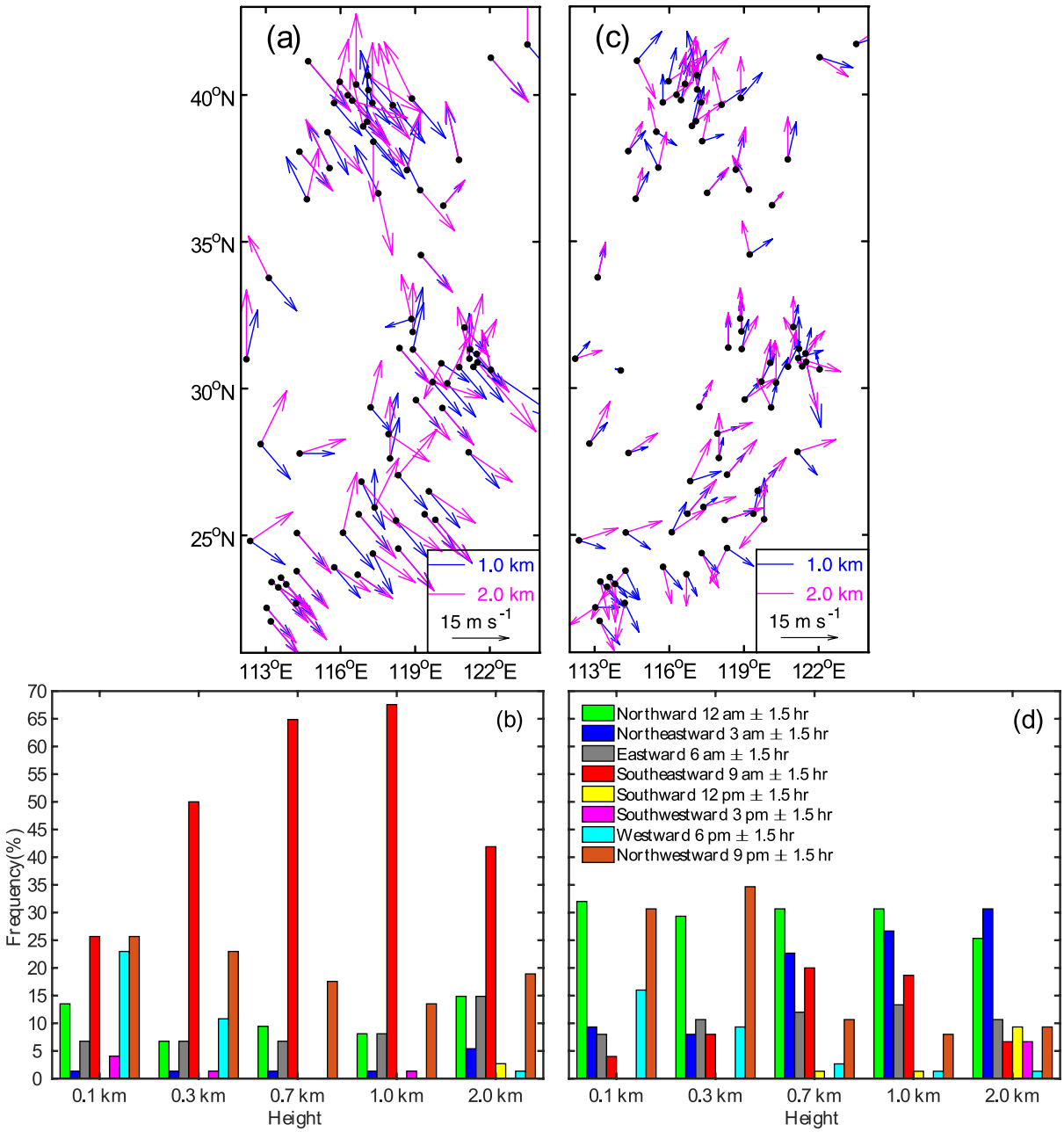

Figure 4. (a) The most frequent occurrence time (arrow direction following a standard 24-hr clock) and magnitude (arrow length in m s^{-1}) of maximum hourly wind speed at 1 (blue arrows) and 2 (magenta arrows) km above ground level (AGL) for each wind profiler radar (WPR) site in eastern China. For the standard 24-hr clock convention used here, magenta the northward, eastward, southward, and westward vectors denote the 12:00 a.m., 6:00 a.m., 12:00 p.m., and 6:00 p.m. local time, respectively. Panel (c) as in panel (a), except we first calculate the mean diurnal cycle of hourly wind speed for each site at 1 and 2 km AGL, then get the local time and magnitude of the maximum hourly mean wind speed. (b), (d) Frequency distribution of local time results over all sites in (a) and (c), respectively, and the corresponding results at 0.1, 0.3, 0.7, 1.0, and 2.0 km AGL (colored according to the key in the upper left of panel d). The corresponding results of panels (a) and (c) over all WPR sites in China are provided in Figure S3 in Supporting Information S1.

stations. Figure S7 in Supporting Information S1 shows that the differences between median WS_{wpr} and median WS_{rad} generally range from around −2 m s^{-1} to near zero. Both WS_{wpr} and WS_{rad} exhibit similar variations with increasing height. However, larger deviations between WS_{wpr} and WS_{rad} are observed at the coastal site (Sanya) compared to the inland site (Beijing) and small island site (Xisha). These differences can be attributed to several factors. First, the distance between the WPR and radiosonde sites can span dozens of kilometers, and the notable heterogeneity of the underlying surface in coastal areas introduces representativeness errors, making the

comparison of WPR and radiosonde data difficult particularly near the surface (Miao et al., 2018). This effect diminishes with increasing height (Figure S7 in Supporting Information S1). Second, while radiosonde data provide reliable point measurements, WPR measurements are influenced by precipitation processes and represent the horizontal average over approximately 253 and 506 m at 1 and 2 km AGL heights, respectively, as estimated based on the horizontal distance between vertical and off-vertical beams (May, 1993).

3.3. Discussion

As the WPR provides hourly wind data, we briefly assess the ERA5 reanalysis (that did not assimilate these WPR data) for comparison. The $S(f)$ derived from ERA5, $S_{EC}(f)$, accurately reproduces spectral features for $f < 10^{-5}$ s^{-1} which corresponds to time scales greater than 1 day (Figure 2), as well as the spatial distribution of slopes in Range-1 (Figure 1d). For instance, the mean and standard deviation of slopes over the six heights at five sites in Figure 2 are -0.08 ± 0.01 and -0.06 ± 0.02 for the WPR and ERA5, respectively. The slopes of $S_{EC}(f)$ in Range-2 and Range-3 exhibit similar spatial patterns to those of $S_{WPR}(f)$ (Figures 1e and 1f), demonstrating the overall excellent performance of ERA5 in characterizing large-scale wind fields. However, the spectrum of $S_{EC}(f)$ significantly deviates from that of $S_{WPR}(f)$ for time scales <1 day (Figure 2), resulting in smaller (more negative) slopes in Range-2 and considerably smaller slopes in Range-3 (Figure S2 in Supporting Information S1). This is consistent with the finding of Skamarock (2004) from numerical modeling tests, showing that the model's spectra decay at the highest resolved wavenumbers (or frequency) compared to observations, likely due to energy removal by the model's dissipation mechanisms. Similarly, Bolgiani et al. (2022) found that, while properly capturing the synoptic conditions and seasonal variability, ERA5's wind spectra are not able to properly reproduce the dissipation rates at the mesoscale.

One consequence of the deficiency of $S_{EC}(f)$ for time scales <1 day, we hypothesize, is that the ERA5 may have difficulty in reproducing the LLJ with a short duration (e.g., less than 12 hr). As a preliminary test, Figure S8 in Supporting Information S1 compares the LLJ height and occurrence time between WPR and ERA5 at Sanya for 11–20 August 2019. Indeed, ERA5 performs better in capturing the LLJ with a relatively long duration from 11 to 15 August than in reproducing the LLJ with a relatively short duration from 16 to 20 August. To improve the performance of ERA5 reanalysis for its $S_{EC}(f)$ for time scales <1 day and for LLJ cases, assimilation of the WPR data, improvement in model physical parameterizations, and increasing the horizontal resolution will likely be helpful. Indeed, the WPR data in China have been successfully assimilated into a regional model, and the combined assimilation of both WPR and Doppler radar enhances the analysis and forecasting of wind (C. Wang et al., 2022, 2023).

4. Summary

The WPR data from the network of 91 operational stations of the CMA have been used to investigate the synoptic and mesoscale spectrum of winds, as well as the maximum wind speed in the lower troposphere and low level jet (LLJ). The power spectral density of winds [$S(f)$] exhibits a slight decrease with frequency f in Range-1 (2×10^{-7} Hz $< f < 1 \times 10^{-6}$ Hz; or 12 days to 1 month). In Range-2 (3×10^{-6} Hz $< f < 2 \times 10^{-5}$ Hz; or 14 hr to 4 days) and Range-3 (2×10^{-5} Hz $< f < 1.3 \times 10^{-4}$ Hz; or 2–14 hr), the slopes of $S_{WPR}(f)$ approximately follow a $f^{-5/3}$ power law over the ocean; however, they significantly exceed −5/3 in inland areas.

The maximum wind speeds in the north plain and northeastern regions of China range from 15 to 16.5 m s^{-1}, while in other regions, they generally do not exceed 15 m s^{-1}. LLJs in the inland region in southern China occur preferentially at higher altitudes (>1.2 km AGL) compared to other regions. Comparatively, the timing of the maximum wind speed in southern China occurs several hours later than in northern China, partially due to the increased inertial period associated with decreasing latitudes.

Through a case study conducted at two coastal sites, we demonstrated the influence of horizontal temperature gradients and the resulting thermal wind on the timing and magnitude of LLJs. Additionally, we compared WPR wind speeds with radiosonde data from the same hour at three sites (inland, coastal, and small island), and the observed differences primarily arise from the distances between the WPR and radiosonde sites, as well as the surface inhomogeneities, particularly over the coastal site.

We also used the WPR data to conduct a brief evaluation of the ERA5 reanalysis. Our findings indicate that the ERA5 reanalysis performs exceptionally well in reproducing the wind spectrum for time scales exceeding

1 day. However, we observed significant discrepancies between the profiler data and the $S_{EC}(f)$ at shorter time scales. One consequence is the difficulty of the ERA5 reanalysis in capturing short-duration LLJs. Conducting a comprehensive evaluation of various existing reanalysis wind data using the WPR measurements will be a part of our future work.

This study does not include the analysis of horizontal wind variation on the microscale due to the limited time resolution of the WPR data (5–6 min of the raw data, averaged into hourly data used here). To delve into this aspect and bridge the gap between microscale and mesoscale, wind lidar measurements with high time resolution (~1 Hz) would be necessary. The CMA has plans to establish a wind lidar network in China. By combining the data from the WPR and wind lidar measurements, we will be able to analyze the full-scale spectrum of wind in clear sky region in the lower troposphere over China in the near future.

Data Availability Statement

The radiosonde data at specific isobaric levels are from the China National Meteorological Information Center (http://data.cma.cn/en), the users need to register an account, and then refer to the introductions in link http://data.cma.cn/en/?r=article/getLeft/id/343/keyIndex/30. The wind profiler radar and L-band radiosonde data are not publicly available due to access constraints imposed by CMA. ERA5 reanalysis data are from European Centre for Medium-Range Weather Forecasts (https://cds.climate.copernicus.eu/cdsapp#!/home), and the public processed data can be obtained at https://www.scidb.cn/s/EBNvai.

Acknowledgments
We thank two anonymous reviewers for constructive comments and suggestions that have helped our revision. Wang and Xu are supported by the Second Tibetan Plateau Scientific Expedition and Research (STEP) program (2019QZKK0105). Wang is also supported by Basic Research Fund of Chinese Academy of Meteorological Sciences (2023Z008), Science and Technology Development Foundation of Chinese Academy of Meteorological Sciences (2023KJ042), and the National Natural Science Foundation of China under Grant 42375015.

References

Blackadar, A. K. (1957). Boundary layer wind maxima and their significance for the growth of nocturnal inversions. *Bulletin of the American Meteorological Society*, *38*(5), 283–290. https://doi.org/10.1175/1520-0477-38.5.283

Bolgiani, P., Calvo-Sancho, C., Díaz-Fernández, J., Quitián-Hernández, L., Sastre, M., Santos-Muñoz, D., et al. (2022). Wind kinetic energy climatology and effective resolution for the ERA5 reanalysis. *Climate Dynamics*, *59*(3–4), 737–752. https://doi.org/10.1007/s00382-022-06154-y

Bonner, W. D., Esbensen, S., & Greenberg, R. (1968). Kinematics of the low-level jet. *Journal of Applied Meteorology*, *7*(3), 339–347. https://doi.org/10.1175/1520-0450(1968)007<0339:KOTLLJ>2.0.CO;2

Burrows, D. A., Ferguson, C. R., & Bosart, L. F. (2020). The role of upper-level coupling on Great Plains low-level jet structure and variability. *Journal of the Atmospheric Sciences*, *77*(12), 4317–4335. https://doi.org/10.1175/JAS-D-20-0059.1

Callies, J., Ferrari, R., & Bühler, O. (2014). Transition from geostrophic turbulence to inertia–gravity waves in the atmospheric energy spectrum. *Proceedings of the National Academy of Sciences*, *111*(48), 17033–17038. https://doi.org/10.1073/pnas.1410772111

Climatological Atlas. (2002). *Climatological Atlas of the People's Republic of China*. China Meteorological Press, by the Editorial committee of Climatological Atlas of the People's Republic of China.

Du, Y., Zhang, Q., Chen, Y., Zhao, Y., & Wang, X. (2014). Numerical simulations of spatial distributions and diurnal variations of low-level jets in China during early summer. *Journal of Climate*, *27*(15), 5747–5767. https://doi.org/10.1175/JCLI-D-13-00571.1

Guo, J., Miao, Y., Zhang, Y., Liu, H., Li, Z., Zhang, W., et al. (2016). The climatology of planetary boundary layer height in China derived from radiosonde and reanalysis data. *Atmospheric Chemistry and Physics*, *16*(20), 13309–13319. https://doi.org/10.5194/acp-16-13309-2016

Gutierrez, W., Araya, G., Kiliyanpilakkil, P., Ruiz-Columbie, A., Tutkun, M., & Castillo, L. (2016). Structural impact assessment of low level jets over wind turbines. *Journal of Renewable and Sustainable Energy*, *8*(2), 023308. https://doi.org/10.1063/1.4945359

Heggem, T., Lende, R., & Løvseth, J. (1998). Analysis of long time series of coastal wind. *Journal of the Atmospheric Sciences*, *55*(18), 2907–2917. https://doi.org/10.1175/1520-0469(1998)055<2907:AOLTSO>2.0.CO;2

Hersbach, H., Bell, B., Berrisford, P., Hirahara, S., Horányi, A., Muñoz-Sabater, J., et al. (2020). The ERA5 global reanalysis. *Quarterly Journal of the Royal Meteorological Society*, *146*(730), 1999–2049. https://doi.org/10.1002/qj.3803

Högström, U., Sahlée, E., Smedman, A.-S., Rutgersson, A., Nilsson, E., Kahma, K. K., & Drennan, W. M. (2015). Surface stress over the ocean in swell-dominated conditions during moderate winds. *Journal of the Atmospheric Sciences*, *72*(12), 4777–4795. https://doi.org/10.1175/JAS-D-15-0139.1

Kaplan, M. L., Lin, Y.-L., Charney, J. J., Pfeiffer, K. D., Ensley, D. B., DeCroix, D. S., & Weglarz, R. P. (2000). A terminal area PBL prediction—System at Dallas–Fort worth and its application in simulating diurnal PBL jets. *Bulletin of the American Meteorological Society*, *81*(9), 2179–2204. https://doi.org/10.1175/1520-0477(2000)081<2179:ATAPPS>2.3.CO;2

Koch, S. E., Fengler, M., Chilson, P. B., Elmore, K. L., Argrow, B., Andra, D. L., & Lindley, T. (2018). On the use of unmanned aircraft for sampling mesoscale phenomena in the preconvective boundary layer. *Journal of Atmospheric and Oceanic Technology*, *35*(11), 2265–2288. https://doi.org/10.1175/JTECH-D-18-0101.1

Larsén, X. G., Larsen, S. E., & Petersen, E. L. (2016). Full-scale spectrum of boundary-layer winds. *Boundary-Layer Meteorology*, *159*(2), 349–371. https://doi.org/10.1007/s10546-016-0129-x

Larsén, X. G., Petersen, E. L., & Larsen, S. E. (2018). Variation of boundary-layer wind spectra with height. *Quarterly Journal of the Royal Meteorological Society*, *144*(716), 2054–2066. https://doi.org/10.1002/qj.3301

Larsén, X. G., Vincent, C., & Larsen, S. (2013). Spectral structure of mesoscale winds over the water. *Quarterly Journal of the Royal Meteorological Society*, *139*(672), 685–700. https://doi.org/10.1002/qj.2003

Li, B., Li, C., Yang, Q., Tian, Y., & Zhang, X. (2021). Full-scale wind speed spectra of 5 Year time series in urban boundary layer observed on a 325 m meteorological tower. *Journal of Wind Engineering and Industrial Aerodynamics*, *218*, 104791. https://doi.org/10.1016/j.jweia.2021.104791

Lindborg, E. (1999). Can the atmospheric kinetic energy spectrum be explained by two-dimensional turbulence? *Journal of Fluid Mechanics*, *388*, 259–288. https://doi.org/10.1017/S0022112099004851

Liu, B., Guo, J., Gong, W., Shi, L., Zhang, Y., & Ma, Y. (2020). Characteristics and performance of wind profiles as observed by the radar wind profiler network of China. *Atmospheric Measurement Techniques*, *13*(8), 4589–4600. https://doi.org/10.5194/amt-13-4589-2020

Markowski, P., & Richardson, Y. (2010). *Mesoscale meteorology in midlatitudes* (p. 407). Wiley-Blackwell.
May, P. T. (1993). Comparison of wind-profiler and radiosonde measurements in the tropics. *Journal of Atmospheric and Oceanic Technology*, *10*(1), 122–127. https://doi.org/10.1175/1520-0426(1993)010<0122:COWPAR>2.0.CO;2
Miao, Y., Guo, J., Liu, S., Wei, W., Zhang, G., Lin, Y., & Zhai, P. (2018). The climatology of low-level jet in Beijing and Guangzhou, China. *Journal of Geophysical Research: Atmospheres*, *123*(5), 2816–2830. https://doi.org/10.1002/2017JD027321
Nastrom, G. D., Fritts, D. C., & Gage, K. S. (1987). An investigation of terrain effects on the mesoscale spectrum of atmospheric motions. *Journal of the Atmospheric Sciences*, *44*(20), 3087–3096. https://doi.org/10.1175/1520-0469(1987)044<3087:AIOTEO>2.0.CO;2
Parish, T. R., & Oolman, L. D. (2010). On the role of sloping terrain in the forcing of the Great Plains low-level jet. *Journal of the Atmospheric Sciences*, *67*(8), 2690–2699. https://doi.org/10.1175/2010JAS3368.1
Ranjha, R., Svensson, G., Tjernström, M., & Semedo, A. (2013). Global distribution and seasonal variability of coastal low-level jets derived from ERA-Interim reanalysis. *Tellus A: Dynamic Meteorology and Oceanography*, *65*(1), 20412. https://doi.org/10.3402/tellusa.v65i0.20412
Rife, D. L., Pinto, J. O., Monaghan, A. J., Davis, C. A., & Hannan, J. R. (2010). Global distribution and characteristics of diurnally varying low-level jets. *Journal of Climate*, *23*(19), 5041–5064. https://doi.org/10.1175/2010JCLI3514.1
Shapiro, A., & Fedorovich, E. (2010). Analytical description of a nocturnal low-level jet: Analytical description of a nocturnal low-level jet. *Quarterly Journal of the Royal Meteorological Society*, *136*(650), 1255–1262. https://doi.org/10.1002/qj.628
Shapiro, A., Fedorovich, E., & Rahimi, S. (2016). A unified theory for the Great plains nocturnal low-level jet. *Journal of the Atmospheric Sciences*, *73*(8), 3037–3057. https://doi.org/10.1175/JAS-D-15-0307.1
Sim, S.-K., Peinke, J., & Maass, P. (2023). Signatures of geostrophic turbulence in power spectra and third-order-structure function of offshore wind speed fluctuations. *Scientific Report*, *13*, 13411. https://doi.org/10.1038/s41598-023-40450-9
Skamarock, W. C. (2004). Evaluating mesoscale NWP models using kinetic energy spectra. *Monthly Weather Review*, *132*(12), 3019–3032. https://doi.org/10.1175/MWR2830.1
Smedman, A.-S. (1991). Occurrence of roll circulations in a shallow boundary layer. *Boundary-Layer Meteorology*, *57*(4), 343–358. https://doi.org/10.1007/BF00120053
Smedman, A.-S., Bergström, H., & Högström, U. (1995). Spectra, variances and length scales in a marine stable boundary layer dominated by a low level jet. *Boundary-Layer Meteorology*, *76*(3), 211–232. https://doi.org/10.1007/BF00709352
Storm, B., Dudhia, J., Basu, S., Swift, A., & Giammanco, I. (2009). Evaluation of the Weather Research and Forecasting model on forecasting low-level jets: Implications for wind energy. *Wind Energy*, *12*(1), 81–90. https://doi.org/10.1002/we.288
Walters, C. K., Winkler, J. A., Shadbolt, R. P., van Ravensway, J., & Bierly, G. D. (2008). A long-term climatology of southerly and northerly low-level jets for the Central United States. *Annals of the Association of American Geographers*, *98*(3), 521–552. https://doi.org/10.1080/00045600802046387
Wang, C., Chen, M., & Chen, Y. (2022). Impact of combined assimilation of wind profiler and Doppler radar data on a convective-scale cycling forecasting system. *Monthly Weather Review*, *150*(2), 431–450. https://doi.org/10.1175/MWR-D-20-0383.1
Wang, C., Chen, Y., Chen, M., & Huang, X.-Y. (2023). Evaluation of two observation operator schemes for wind profiler radar data assimilation and its impacts on short-term forecasting. *Atmospheric Research*, *283*, 106549. https://doi.org/10.1016/j.atmosres.2022.106549
Wang, Y., Zhang, L., Peng, J., & Liu, S. (2018). Mesoscale horizontal kinetic energy spectra of a tropical cyclone. *Journal of the Atmospheric Sciences*, *75*(10), 3579–3596. https://doi.org/10.1175/JAS-D-17-0391.1
Wei, W., Zhang, H. S., & Ye, X. X. (2014). Comparison of low-level jets along the north coast of China in summer. *Journal of Geophysical Research: Atmospheres*, *119*(16), 9692–9706. https://doi.org/10.1002/2014JD021476
Welch, P. (1967). The use of fast fourier transform for the estimation of power spectra: A method based on time averaging over short, modified periodograms. *IEEE Transactions on Audio and Electroacoustics*, *15*(2), 70–73. https://doi.org/10.1109/TAU.1967.1161901
Whiteman, C. D., Bian, X., & Zhong, S. (1997). Low-level jet climatology from enhanced Rawinsonde observations at a site in the southern Great Plains. *Journal of Applied Meteorology*, *36*(10), 1363–1376. https://doi.org/10.1175/1520-0450(1997)036<1363:LLJCFE>2.0.CO;2
Yan, Y., Cai, X., Wang, X., Miao, Y., & Song, Y. (2021). Low-level jet climatology of China derived from long-term radiosonde observations. *Journal of Geophysical Research: Atmospheres*, *126*(20), e2021JD035323. https://doi.org/10.1029/2021JD035323
Yepes, J., Poveda, G., Mejía, J. F., Moreno, L., & Rueda, C. (2019). CHOCO-JEX: A research experiment focused on the Chocó low-level jet over the far eastern Pacific and western Colombia. *Bulletin of the American Meteorological Society*, *100*(5), 779–796. https://doi.org/10.1175/BAMS-D-18-0045.1
Zhang, W., Guo, J., Miao, Y., Liu, H., Song, Y., Fang, Z., et al. (2018). On the summertime planetary boundary layer with different thermodynamic stability in China: A radiosonde perspective. *Journal of Climate*, *31*(4), 1451–1465. https://doi.org/10.1175/JCLI-D-17-0231.1